# Features of Afterbody Radiative Heating for Earth Entry

Christopher O. Johnston*
*NASA Langley Research Center, Hampton, VA 23681*
and
Aaron M. Brandis†
*ERC Corporation at NASA Ames, Mountain View, CA 94035*

**Radiative heating is identified as a major contributor to afterbody heating for Earth entry capsules at velocities above 10 km/s. Because of rate-limited electron-ion recombination processes, a large fraction of the electronically-excited N and O atoms produced in the high temperature/pressure forebody remain as they expand into the afterbody region, which results in significant afterbody radiation. Large radiative heating sensitivities to electron-impact ionization rates and escape factors are identified. Ablation products from a forebody ablator are shown to increase the afterbody radiation by as much as 40%. The tangent-slab radiation transport approach is shown to over-predict the radiative flux by as much as 40% in the afterbody, therefore making the more computationally expensive ray-tracing approach necessary for accurate radiative flux predictions. For the Stardust entry, the afterbody radiation is predicted to be nearly twice as large as the convective heating during the peak heating phase of the trajectory. Comparisons between simulations and the Stardust Echelle observation measurements, which are shown to be dominated by afterbody emission, indicate agreement within 20% for various N and O lines. Similarly, calorimeter measurements from the Fire II experiment are identified as a source of validation data for afterbody radiation. For the afterbody calorimeter measurement closest to the forebody, which experiences the largest afterbody radiative heating component, the convective heating alone is shown to under-predict the measurement, even for the fully-catalytic assumption. Agreement with the measurements is improved with the addition of afterbody radiation. These comparisons with Stardust and Fire II measurements provide validation that the significant afterbody radiation values proposed in this work are legitimate.**

## I. Introduction

This paper investigates the simulation of shock-layer radiative heating to the afterbody surface of reentry capsules entering Earth at velocities greater than 10 km/s. Because afterbody radiometers on Fire II and Apollo 4 and 6 measured negligible values,[1] it has typically been assumed that afterbody radiation for Earth entry is small or negligible relative to convective heating, and has therefore received limited attention. When afterbody radiation has been considered, either a Boltzmann distribution of electronic states was assumed[2–4] or the vacuum ultraviolet contribution was ignored.[5] As will be shown in this paper, the small afterbody radiative heating relative to convective heating resulting from these assumptions is potentially in serious error.

This observation does not contradict the negligible Fire and Apollo measurements for two reasons. First, these measurements did not capture the vacuum ultraviolet (VUV) region of the spectrum, which will be shown in this paper to contribute up to 7 times the non-VUV radiative flux. Second, these measurements had a lower sensitivity limit of roughly 2 W/cm$^2$, below which the radiometer read a value of zero. Therefore, a

*Aerospace Engineer
†Associate Research Scientist, AIAA Professional Member

radiometer location that encountered just under 2 W/cm$^2$ of non-VUV radiative flux, and therefore produced a negligible radiometer reading, could have actually encountered 14 W/cm$^2$ of VUV and 16 W/cm$^2$ of total radiative flux. This value may be nearly equal to, if not greater than, the convective heating for most afterbody flows, and is certainly not negligible. While no direct experimental data exist to confirm this strong afterbody VUV flux, this paper will show that the Fire II afterbody calorimeters provide evidence of significant radiative flux.

To elucidate the physics of this strong afterbody radiative heating, Section II presents a simplified approach for connecting the nonequilibrium afterbody flowfield to the non-Boltzmann model and radiative spectrum. This will provide insight into the strong VUV contribution mentioned in the previous paragraph, which is significantly different than that seen in strongly equilibrium forebody flows.[6] Section III examines the impact of the escape factor, which represents the largest uncertainty for the collisional radiative model, and the impact of the three-body electron-ion recombination rate, which represents the largest uncertainty for the flowfield model. Section IV examines the contribution of radiative heating to the afterbody of the Stardust capsule, and comparisons are made to the Echelle observation measurements. Finally, Section V presents the comparisons between the present model and the Fire II calorimeter data mentioned above.

## II. Afterbody Radiative Heating Overview for Earth Entry

This section provides a fundamental analysis of afterbody radiation for Earth entry. Relevant spectrum and non-Boltzmann model details, including a review of the optically-thick limit in nonequilibrium flow, are presented first in subsection A, while relevant flowfield characteristics, which drive the spectrum and non-Boltzmann models, are presented in subsection B.

### A. Features of the Spectrum and Electronic State Population Distribution

To identify the dominant contributors to afterbody radiative heating for Earth entry, the intensity along a 15 cm constant property line-of-sight is considered. Number densities and temperatures, which are chosen to represent typical afterbody values, are set to the following: [N, O, $N^+$, $O^+$, $e^-$] = [7.50e+15, 2.11e+15, 3.74e+14, 7.95e+13, 4.53e+14] particles/cm$^3$, with $T_{ve}$ = 5231 K and $T_{tr}$ = 5023 K. The radiative intensity spectrum resulting from this constant property line-of-sight is presented in Fig. 1. The VUV is seen to contribute over 85% of the integrated intensity, with 65% resulting from the three VUV lines presented in Table 1. This confirms the strong VUV contribution mentioned in the Introduction. Note that for typical *forebody* radiative heating, the VUV contributes less than 50% of the total radiative flux. An explanation for the significant afterbody VUV component is provided in the following discussion.

Note that the three lines listed in Table 1, as well as all VUV lines for N or O, are the result of electronic transitions between an upper level ($j$) greater than 3 and a lower level ($i$) less than 4, where Table 2 defines these levels for N. The emission and absorption for an atomic line are proportional to the population of the upper and lower level, respectively. Figure 2 presents the population distribution for N along with the corresponding Saha-Boltzmann and Boltzmann distributions. The Saha-Boltzmann distribution for electronic level $i$ is written as:

$$N_i^{SE} = N_+ N_e \frac{g_i}{2Q_+} \left( \frac{h^2}{2\pi m k T_e} \right)^{3/2} exp \left[ \frac{hc(E_{ionize} - E_i)}{kT_e} \right] \tag{1}$$

where $N_+$ is the corresponding ion number density, and $N_e$ is the electron number density, while the the Boltzmann distribution is written as:

$$N_i^B = N_a \frac{g_i}{Q_a} exp \left( -\frac{hc}{kT_e} E_i \right) \tag{2}$$

where $N_a$ is the atom number density and $Q_a$ is the atomic partition function.

Two observations of significant consequence for afterbody radiative heating can be made from Figure 2. The first is that the non-Boltzmann, or collisional-radiative (CR), model prediction for level 5, which is the emitting upper level for the lines of interest, is near the Saha-Boltzmann value, and many orders of magnitude greater than the Boltzmann value. This is opposite of the trend seen in compressing flow, such as that in the post-shock region, where the Saha-Boltzmann values are lower than the Boltzmann values. The second observation from Figure 2 is that the CR model predictions for the absorbing lower three levels are nearly

identical to the Boltzmann values. These observations, which will be shown in the following paragraphs to have significant consequences on the radiative transport, are generally applicable for expanding ionized flow.

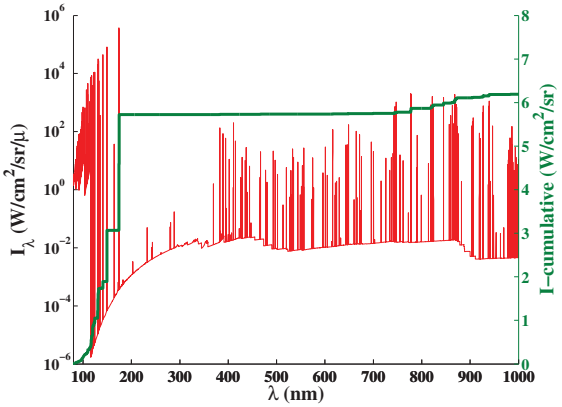


Figure 1: Radiative intensity spectrum for a constant property line-of-sight representative of afterbody flow.

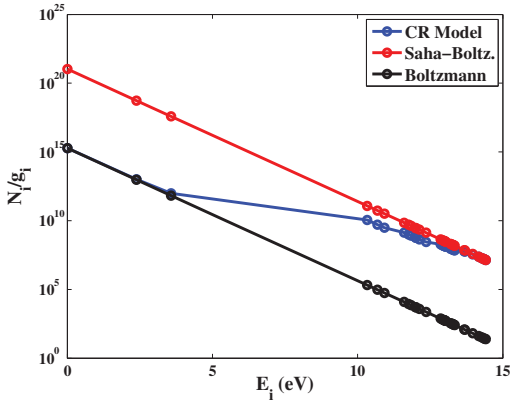


Figure 2: Atomic nitrogen population distribution for the constant property line-of-sight.

Table 1: Atomic lines that provide largest contribution to afterbody radiative heating.

| Species | $\lambda_{CL,mult}$ (nm) | $i$ | $j$ | Wiese ID* | $\pm f_{ij}$ (%) | $\pm\Delta\lambda_{S,0}$ (%) |
|---|---|---|---|---|---|---|
| N | 149.33 | 2 | 5 | 15 | 10 | 30 |
| N | 174.36 | 3 | 5 | 29 | 20 | 50 |
| O | 130.35 | 1 | 5 | 2 | 3 | 50 |

* Multiplet number listed by Wiese et al.[7]

Table 2: First 5 electronic energy levels for atomic nitrogen.

| Level $i$ | $E_i$ (eV) | $g_i$ |
|---|---|---|
| 1 | 0 | 4 |
| 2 | 2.383962 | 10 |
| 3 | 3.575602 | 6 |
| 4 | 10.332297 | 12 |
| 5 | 10.686543 | 6 |

The large VUV component to the radiative intensity seen in Fig. 1 for afterbody conditions is explained by considering the optically-thick limit for a single atomic line transition, which is written as

$$I_{\lambda,Limit} = \frac{2hc^2}{\lambda}\frac{N_j N_i^B}{N_i N_j^B} exp\left(-\frac{hc}{kT_{ve}}\frac{1}{\lambda}\right) \tag{3}$$

Note that when $N_j$ and $N_i$, which are respectively the number densities of the upper and lower levels for the atomic line, are equal to their Boltzmann value, this equation reduces to the Planck function. Values of $I_{\lambda,Limit}$ obtained from Eq. (3) are compared in Fig. 3 with the Planck function and the spectrum, for the constant-property case considered previously. The atomic lines in the VUV are seen to hit the $I_{\lambda,Limit}$ values, which are labelled as the "Nonequil. Limit", while the non-VUV lines are below this limit. Note that a line will be limited by $I_{\lambda,Limit}$ if the following relationship is satisfied

$$exp\left(-N_i\sigma_\nu\Delta z\right) < 0.1 \tag{4}$$

where $\sigma_\nu$ is the absorption cross section and $\Delta z$ is a characteristic length. The main conclusion of Fig. 3 is that the large VUV component to the radiative intensity is the result of the $I_{\lambda,Limit}$ values being many orders-of-magnitude greater for VUV lines than their corresponding Planck function values. For non-VUV lines, the $I_{\lambda,Limit}$ and Planck function are significantly closer.

The reason for these distinct differences between $I_{\lambda,Limit}$ and the Planck function for VUV and non-VUV lines is explained by considering the observations made previously regarding the population distribution of Fig. 2. From these previous observations, the following approximation is made for VUV lines

$$\frac{N_j N_{i,boltz}}{N_i N_{j,boltz}} \approx \frac{N_j^{SB}}{N_j^B} \tag{5}$$

while for non-VUV lines the following is roughly valid:

$$\frac{N_j N_{i,boltz}}{N_i N_{j,boltz}} \approx 1.0 \tag{6}$$

It will be convenient to define a term $\Phi$ as follows

$$\begin{aligned} \Phi &= log_{10}\left(\frac{N_j^{SB}}{N_j^B}\right) \\ &= log_{10}\left[\frac{N_+ N_e}{N_a}\frac{Q_a}{2Q_+}\left(\frac{h^2}{2\pi m k T_e}\right)^{3/2} exp\left(\frac{hc}{kT_e}E_{ionize}\right)\right] \end{aligned} \tag{7}$$

which represents the order of magnitude difference between the Saha-Boltzmann and Boltzmann populations. For example, the value of $\Phi$ for Fig. 2 is 5.76. Using $\Phi$, $I_{\lambda,Limit}$ is written for VUV lines as

$$I_{\lambda,Limit} \approx \frac{2hc^2}{\lambda} 10^{\Phi} exp\left(-\frac{hc}{kT_{ve}}\frac{1}{\lambda}\right) \tag{8}$$

while the appropriate expression for non-VUV lines is obtained by setting $\Phi$ to zero, which reduces $I_{\lambda,Limit}$ to the Planck function. This equation shows that for VUV lines in expanding flow, where $\Phi >> 0$, the optically-thick limit for line centers are approximately $10^{\Phi}$ times greater than the Planck function, while non-VUV lines are roughly limited by the Planck function.

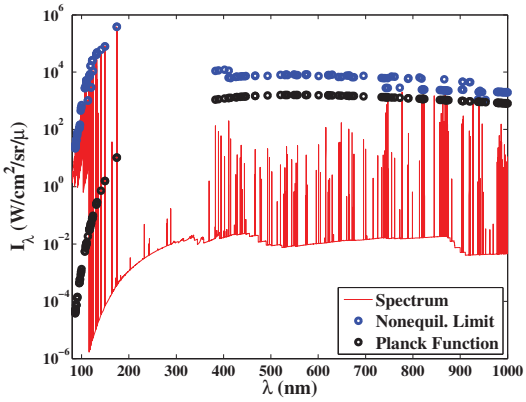


**Figure 3: Radiative flux spectrum and spectral limits for a constant property case.**

In summary, this section provides two significant conclusions for understanding afterbody radiation for Earth entry. The first is that the atomic lines in the VUV provide the dominant contribution, with the three VUV lines listed in Table 1 being especially strong. The second is that afterbody radiation will be largest in regions where both $\Phi >> 0$ and Eq. 4 is satisfied. The next subsection will identify these regions for an actual afterbody flowfield.

### B. Features of the Nonequilibrium Afterbody Flow Relevant to Radiation

Although the high-temperature, ionized flow from the forebody region of a capsule may be in thermochemical equilibrium, the expanding flow around the capsule's shoulder will result in a transition to highly thermochemical nonequilibrium flow.[8,9] This is shown in Fig. 4 and 5, which present the vibrational-electronic

temperature along with the N and $N^+$ number densities for the Stardust capsule at 46 s (11.69 km/s, 1.05e-4 kg/m$^3$). It is seen that between the streamlines bounded by the arrows, relatively significant $N^+$ number densities are present in a region where $T_{ve}$ is as low as 3500 K. This indicates significant chemical nonequilibrium, since at these afterbody temperatures and pressures the chemical equilibrium number density for $N^+$ is less than 1e+10 particles/cm$^3$. Figure 4 also shows that the flow bounded by the arrows, which will be shown to be the strongest radiating region in the afterbody, originates in the forebody. The flow crossing the bow shock in the afterbody region does not provide enough ionization to impact the radiation.

To further quantify the level of nonequilibrium throughout the afterbody, Fig. 6 presents $\Phi$ for the Stardust 46 s case. The region bounded by arrows is the same as that in Figs. 4 and 5, which was identified previously as having non-negligible $N^+$ number density and relatively low $T_{ve}$. As anticipated from the $N^+$ and $T_{ve}$ dependence of $\Phi$ apparent from Eq. (7), this region is seen to have $\Phi$ values greater than 5, indicating a strongly radiating nonequilibrium flow, as discussed in the previous section. A significant fraction of the forebody flow is seen to have $\Phi$ values near zero, indicating chemical equilibrium.

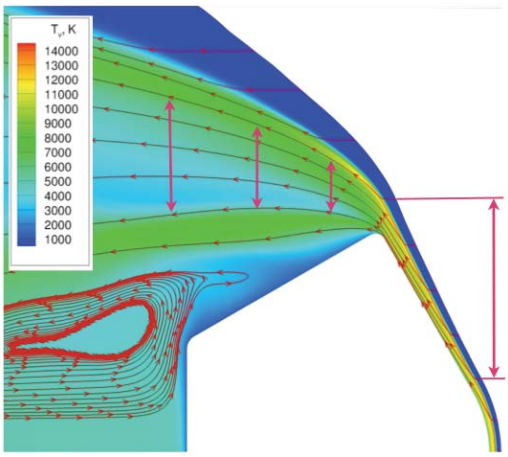


**Figure 4: Vibrational-electronic temperature for Stardust at t = 46 s. The red arrows bound the region that provides the primary afterbody radiation contribution.**

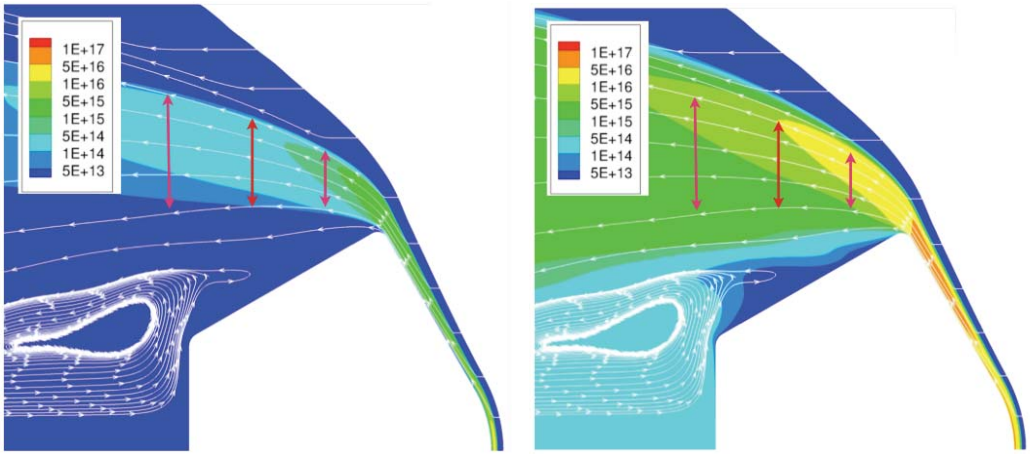


(a) $N^+$ Number Density (particles/cm$^3$) (b) N Number Density (particles/cm$^3$)

**Figure 5: Number densities for Stardust at t = 46 s.**

To examine the radiative heating environment resulting from this flowfield, the radiative intensity along the line-of-sight defined in Fig. 6 is presented in Fig. 7(a). In this figure, where the vehicle surface is located at 0 cm, three distinct regions of radiative transport are seen. Regions of strong emission, strong absorption, and transparency are identified by the slope of the wall-directed radiative intensity. Insight into these regions is provided by the corresponding $\Phi$, temperature, and number density profiles presented in Fig. 7(b)-(c). It is seen that as long as the N number density is greater than roughly 3e+15 particles/cm$^3$, which allows

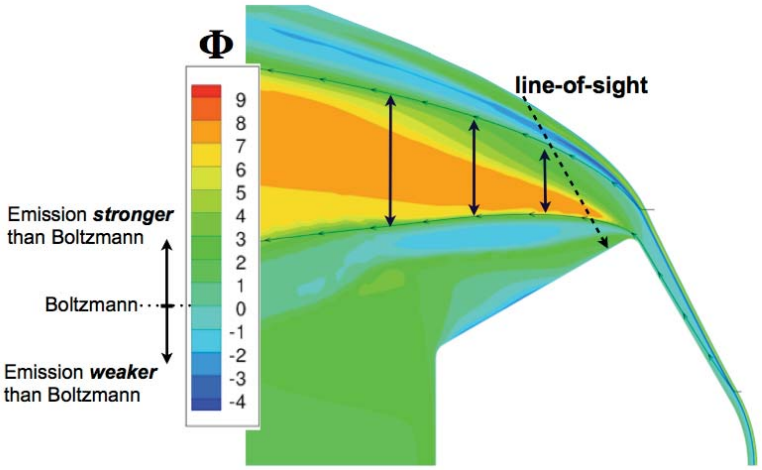


**Figure 6: Values of Φ for Stardust at t = 46 s.**

Eq.(4) to be satisfied, the radiative intensity essential follows Φ, as seen in the strongly emitting region and above 5 cm in the absorbing region. Between 3 and 5 cm, the N number density is still high enough to provide absorption, while Φ is too low for noticeable emission. The transparent region, below 3 cm, occurs when the N number density drops below 1e+15 particles/cm$^3$, which makes absorption negligible.

A notable observation from these figures is that the strongest emission occurs where $T_{ve}$ decreases below 5000 K, while strongest absorption occurs where $T_{ve}$ increases above this value. This counterintuitive result is explained for emission by the positive exponent in Eq. 7, which results in Φ increasing with decreasing temperature. For absorption, increased temperatures result in larger populations for levels 2 and 3 of N, which Table 1 shows are the absorbing levels for the important VUV lines.

## III. Primary Modeling Issues for Afterbody Radiative Heating

While a detailed uncertainty analysis is beyond the scope of the present work, this section examines the modeling issues that are likely the largest contributors to the uncertainty. The identified issues consist of the recombination rate for atomic ions with electrons, the modeling of radiative absorption in the CR model, the influence of forebody ablation products flowing into the afterbody, and three-dimensional radiative transport. These four issues are discussed individually in the following subsections.

### A. Impact of Three-Body Electron-Ion Recombination Rates

The nonequilibrium afterbody regions identified in the previous section, which lead to significant radiation, are primarily the result of the following process: $N^+ + 2e^- \rightarrow N + e^-$, whose rate coefficient is labelled $k_{rec}$. The production rate of N from this process is written as:

$$\frac{\partial N_N}{\partial t} = N_{N+} N_{e-}^2 k_{rec} \tag{9}$$

where $N_{N+}$ and $N_{e-}$ are the $N^+$ and electron number densities, respectively. In most flowfield rate models, including the present, $k_{rec}$ is modeled in terms of the electron-impact-ionization rate ($k_{ion}$) and an equilibrium constant ($K_{equil}$):

$$k_{rec} = \frac{k_{ion}}{K_{equil}} \tag{10}$$

where equilibrium constant is written in terms of the Saha-Boltzmann equation from Eq. 1 as:

$$\frac{1}{K_{equil}} = \frac{1}{N_{N+} N_{e-}} \sum_{i}^{N_L} N_i^{SE} \tag{11}$$

Note that $N_{N+}$ and $N_{e-}$ divide out of this equation, making it a function of only $T_e$. Because $k_{ion}$ is typically provided as a function of only $T_e$, $k_{rec}$ is restricted to this dependence as well. However, Bourdon et al.[10]

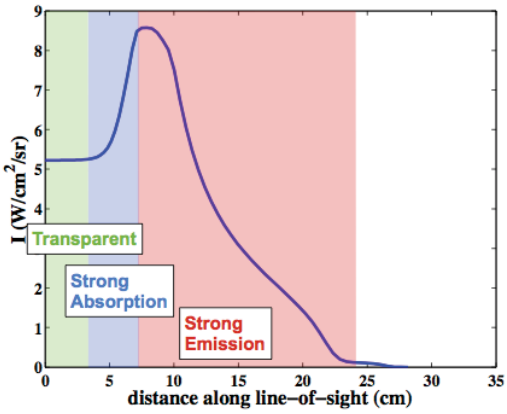


(a) Intensity Profile

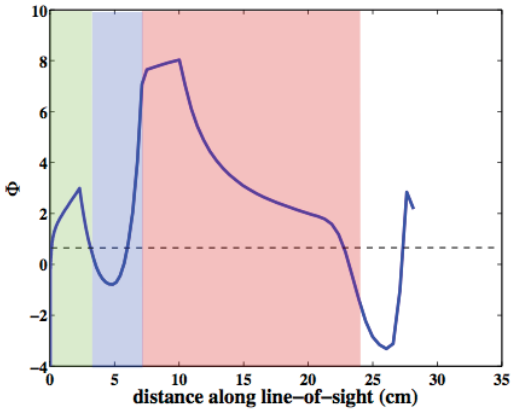


(b) Φ Profile for N

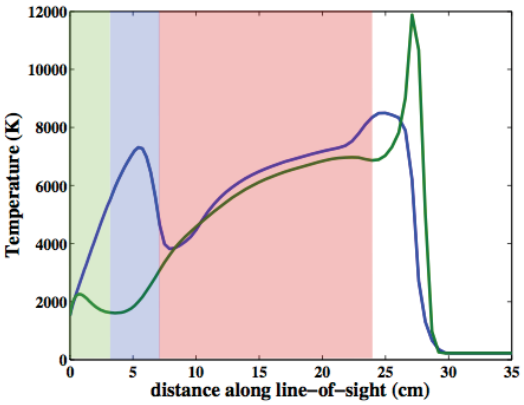


(c) Temperature Profile ($T_{ve}$ = blue, $T_{tr}$ = green)

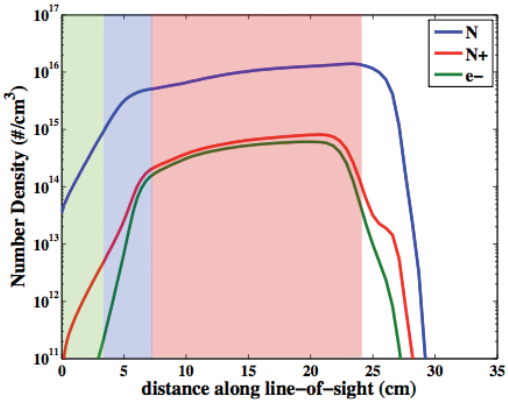


(d) Relevant Number Densities

**Figure 7: Radiation and flowfield properties along line-of-sight defined in Fig. 6.**

show, using a collisional-radiative model, that for non-optically thick conditions, $k_{rec}$ is dependent on $T_e$ as well as the electron number density. Furthermore, Park[11] shows that $k_{rec}$ is also dependent on the strength of radiation throughout the flowfield. Although Park considered the Lyman series of atomic hydrogen, the next subsection of the present work will show that the 174.4 nm line of N provides an influence similar to that shown by Park for the Lyman series.

This lack of $N_{e-}$ and radiative absorption dependence in the flowfield modeling of $k_{rec}$, in addition to minimal available experimental data for $k_{rec}$, results in significant uncertainty in the $k_{rec}$ values applied in flowfield models. A comparison of $k_{rec}$ values suggested by various authors[12–14] and the results of the present CR model are presented in Fig. 8. The Park value is applied in the present flowfield model. Two significant conclusions are made from this figure. The first is that the scatter in proposed rates from the literature is over an order of magnitude. This wide range of possible values represents a major parametric uncertainty for the radiative heating simulations. Second, the impact of the escape factor ($EF$) on the present results is seen to be significant, causing a difference of up to an order-of-magnitude at 10,000 K.

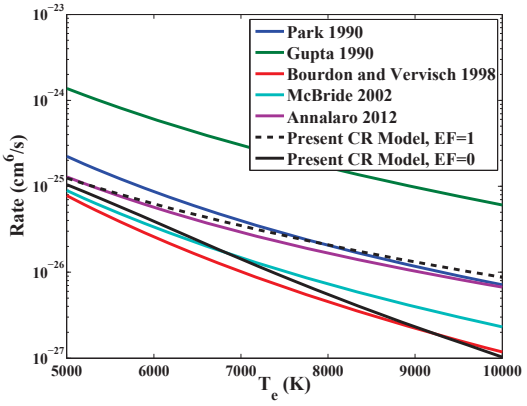


Figure 8: Comparison of recombination rates for $N^+$.

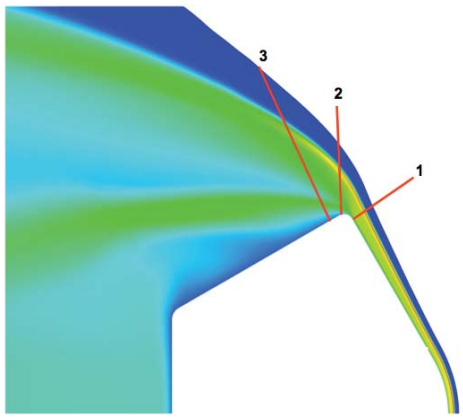


Figure 9: Line of sight definition.

To examine the sensitivity of the afterbody radiation on the tenuous $k_{rec}$ values, Figure 10 compares the results of the nominal $k_{rec}$ values (from Park[12]) with the results of a one-half order-of-magnitude increase in $k_{rec}$ ($k_{ion}$ is increased as well to keep $K_{equil}$ identical). Flowfield and radiation results are plotted along the 3 lines-of-sight presented in Fig. 9. For ray 1, which is still in the compressing forebody regime, the increased $k_{ion}$ results in larger $N^+$ number densities and slightly lower $T_{ve}$ values. The impact of these flowfield changes on the radiative intensity for ray 1 is seen to be negligible. Note that the $\Phi$ values shown in (c) are near zero for ray 1 throughout most the layer (except near the shock and wall), indicating near thermochemical equilibrium. For rays 2 and 3 in the expanding regime, however, the opposite trends in $N^+$ number densities and $T_{ve}$ are seen along most of the line-of-sight. For these cases, the radiative intensity is impacted significantly, with more than a 50% reduction seen for ray 3. These lower radiation values are essentially the result of the reduced $\Phi$ values throughout most of the layer.

## B. Impact of Escape Factors on Collisional-Radiative Modeling

The influence of bound-bound radiative processes on the non-Boltzmann model are represented through terms that capture the influence of emission and absorption. The emission term is written as

$$\left(\frac{\partial N_i}{\partial t}\right)_{em} = \sum_{j=i+1}^{m} A_{ji} N_j - \sum_{j=1}^{i-1} A_{ij} N_i \tag{12}$$

The first term on the right hand side of this equation accounts for the spontaneous emission from atomic lines with an upper level $j$ and lower level $i$, which result in a repopulation of level $i$, while the second term accounts for the spontaneous emission from atomic lines with an upper level $i$ and lower level $j$, which results in a depopulation of level $i$. Implementation of Eq. (12) is straightforward, as $A_{ji}$ and $A_{ij}$ are the Einstein coefficients, which are independent of temperatures and number densities.

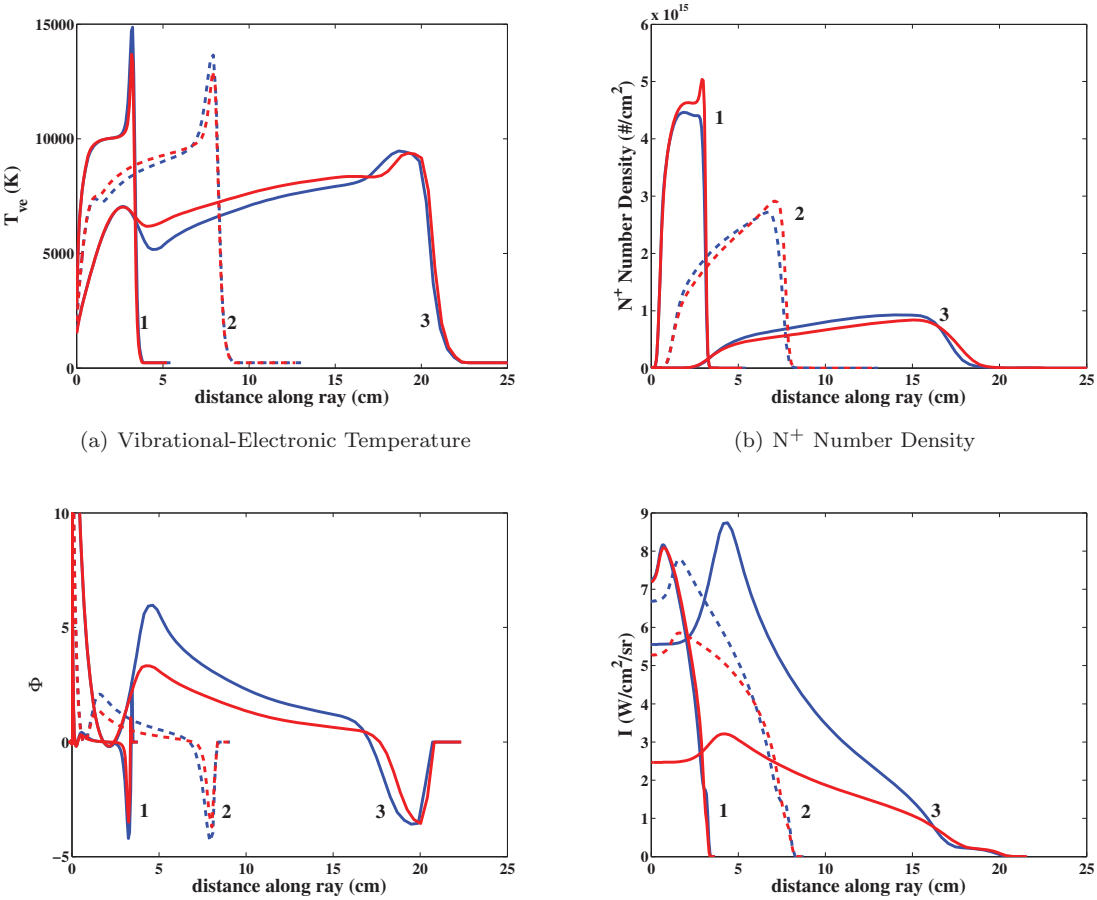


(a) Vibrational-Electronic Temperature

(b) $N^+$ Number Density

(c) Φ for N

(d) Wall-Directed Radiative Intensity

**Figure 10: Flowfield values along the line-of-sight defined in Fig. 9.**

The influence of absorption on the non-Boltzmann model is written as:

$$\left(\frac{\partial N_i}{\partial t}\right)_{abs} = -\sum_{j=i+1}^{m} G_{ji}N_i + \sum_{j=1}^{i-1} G_{ij}N_j \tag{13}$$

where the absorption rate, which depends on the radiative intensity resulting from the entire flowfield ($I_\nu$), is written as

$$G_{ji} = \int_0^\infty \frac{g_j A_{ji} c^4 \int_{4\pi} I_\nu d\Psi}{8\pi h \nu^5} d\nu \tag{14}$$

The evaluation of this term for a variable property tangent-slab is presented in Appendix B of Johnston et al.[15] This term is very computational expensive because it must be evaluated for every atomic line at every frequency and spatial point. Furthermore, treating this term requires numerous iterations. As many as 200 iterations were found to be required for the examples studied in this work.

Because of the difficulty in evaluating Eq. (14), this term is commonly approximated using the escape factor approach. This approach assumes a constant property sphere around the point of interest and only a single atomic line. With these assumptions, Eq. 14 reduces to the following

$$G_{ji} = A_{ji}\frac{N_j}{N_i}(1 - EF_{ji}) \tag{15}$$

where the escape factor, $EF_{ji}$, is defined as

$$EF_{ji} = \int_0^\infty exp(-\kappa_{\nu,ij}\Delta z) d\nu \tag{16}$$

For optically thin lines, $EF_{ji}$ is equal to 1.0, while for optically-thick lines, such as those in the VUV, $EF_{ji}$ is close to 0.0. To show the impact of $EF_{ji}$ on the constant property layer discussed previously in Section A, Figs. 11 and 12 present the population distribution and resulting radiative intensity assuming $EF_{ji}$ values of 1.0 and 0.0 for all atomic nitrogen lines. It is seen that for $EF$=0.0, which represents the optically thick limit, the populations for levels $i$ =4–6 are nearly an order-of-magnitude larger than for $EF$=1.0, which represents the optically thin limit. The impact of these differences in the population distribution on the radiative intensity is shown in Fig. 12, which compares the radiative flux spectrum and resulting cumulative intensity distribution. The larger populations for levels $i$ =4–6 obtained with $EF$=0.0 are seen to result in over a factor of three increase in the total radiative intensity. Most of this increase is produced by nitrogen lines at 120.0, 149.3, and 174.4 nm, which represent transitions between electronic levels 4–1, 5–2, and 5–3, respectively. As expected, these VUV lines emit from levels that are influenced most by the escape factor. Note that the nearly order-of-magnitude increase in the population for these emitting levels shown in Fig. 11 results in nearly a proportional increase in the radiative flux through Eq. (8).

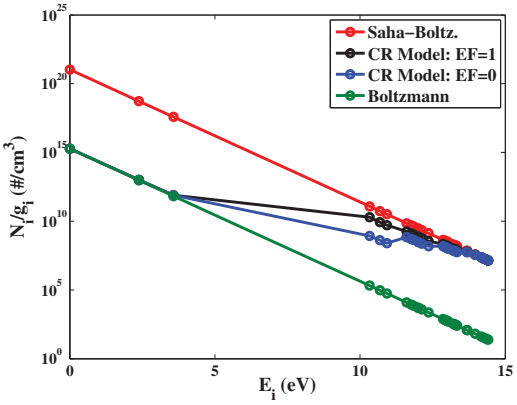


Figure 11: Atomic nitrogen population distribution.

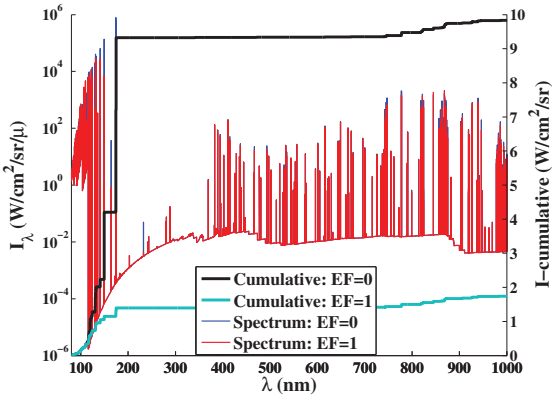


Figure 12: Radiative flux spectrum and spectral limits for a constant property layer representative of afterbody flow.

The escape factor approach provides a good approximation for a constant property layer, if $\Delta z$ is chosen as the thickness of the layer. However, for property layers with separate regions of strong emission and strong absorption, this approach may result in significant error. To examine this possible error, a simplified

flowfield, consisting of the two constant property layers presented in Fig. 13, is considered. This simplified flowfield approximates the actual afterbody flowfield presented in Fig. 7. The production rates of the 5th level of N due to emission (Eq. (12)) and absorption (Eq. (13)) are presented in Fig. 14(a), while the number density of this level are presented in Fig. 14(b). The detailed treatment of $G_{ji}$, which requires 100 iterations, is seen in Fig. 14(a) to result in a significantly larger absorption than the $EF$ treatment below 3 cm (layer A). This absorption results in the significantly higher populations below 3 cm shown in Fig. 14(b), where the populations are actually larger than the Saha-Boltzmann values. The population of all electronic levels of N at 2 cm are presented in Fig. 14(c). A comparison of the radiative intensity profiles obtained with the detailed $G_{ji}$ and approximate $EF$ treatment are compared in Fig. 14(d). The larger excited state number densities below 3 cm are seen to result in less absorption and 26% more radiative intensity reaching the wall.

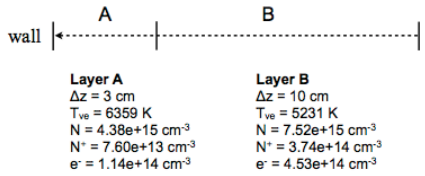


**Figure 13: Dual layer slab definition.**

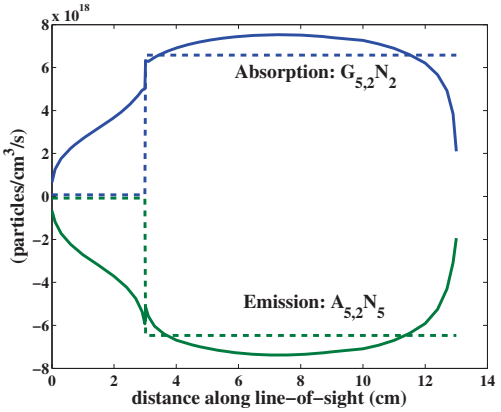


(a) Emission and absorption production rates for the 5th level of N

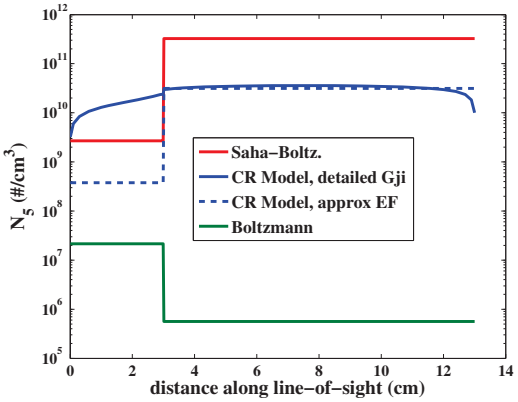


(b) Population distribution for the 5th level of N

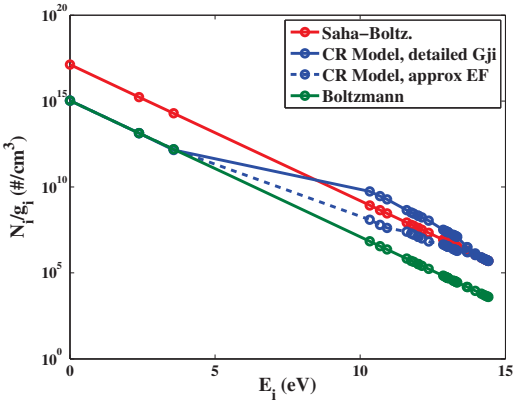


(c) Population distribution for N at 2 cm.

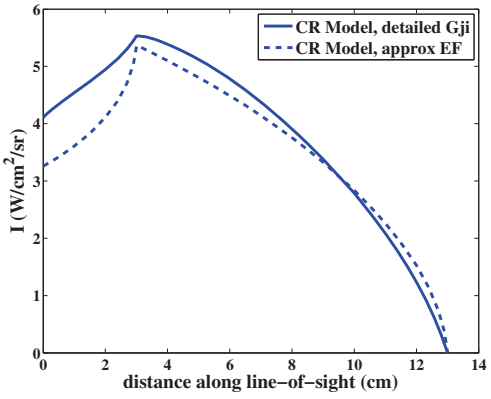


(d) Wall-Directed Radiative Intensity

**Figure 14: Dual layer slab results using the detailed $G_{ji}$ (solid lines) and approximate EF (dashed lines) treatment.**

Applying the detailed $G_{ji}$ approach, although beyond the scope of the present work, should be considered in future studies. This iterative approach is very computationally expensive, which makes the ray tracing

approach required for computing the radiative flux difficult to perform. The present simplified case shows that nearly a 30% error is introduced with the escape factor approximation.

### C. Impact of Forebody Ablation

If an ablating forebody heat shield is present on a vehicle, the chemical species present in the afterbody flow are altered significantly, which influence the afterbody radiative heating. To show this influence for the Stardust 46 s case, a coupled ablation solution was computed assuming steady-state, equilibrium PICA ablation on the forebody. The following 27 species were treated throughout the flowfield: N, $N^+$, NO, $NO^+$, $N_2$, $N_2{}^+$, O, $O^+$, $O_2$, $O_2{}^+$, $e^-$, C, $C^+$, CO, $CO^+$, $CO_2$, $C_2$, $C_3$, $C_5$, $C_2H$, $C_2H_2$, CN, H, $H^+$, $H_2$, HCN, CH. The non-ablating afterbody is assumed in radiative equilibrium and fully-catalytic to homogenous recombination. Figure 15 identifies the ablating forebody and non-ablating afterbody, along with the resulting CO mass fractions.

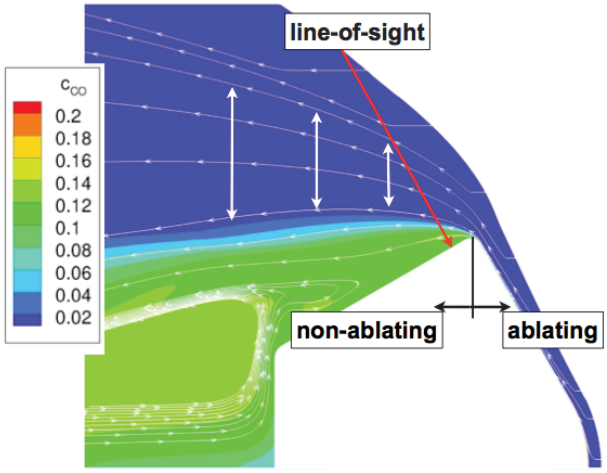


**Figure 15: CO mass fractions and line-of-sight definition for the ablating Stardust 46 s case.**

The impact of ablation on the line-of-sight defined in Fig. 15 is presented in Fig. 16. The mass fraction profiles of relevant species are presented in Fig. 16(a), where ablation products are identified as dashed lines. It is seen that CO is the dominant ablation product, with a peak value of 0.12. As shown in Fig. 15, CO is the result forebody ablation products flowing into the afterbody. The impact of these ablation products on the temperature profiles is shown in Fig. 16(b), which compares the ablating and non-ablating $T_{ve}$ profiles. It is seen that ablation products flowing into the afterbody decreases $T_{ve}$ between 0 and 10 cm. These lower temperatures for the ablating case are seen in Fig. 16(c) to result in larger $\Phi$ values. Because these larger $\Phi$ values occur in the strongly absorbing region identified previously in Fig. 7(b), significantly less absorption is expected for the ablating case. This reduced absorption, and therefore larger radiative intensity reaching the surface, is shown in Fig. 16(d). A 40% larger radiative intensity is seen at the surface for the ablating case. Note that this larger radiative intensity for the ablating case is not the result of emission from ablation products, such as CO, but rather the influence of the ablation products on the vibrational-electronic energy equation. This is confirmed in Figure 17, which compares the intensity spectrum for the ablating and non-ablating cases. It is seen that the increased intensity for the ablating case comes from increased emission from the VUV lines identified previously for air, while no new molecular bands from ablation products are noticeable.

### D. Three-Dimensional Radiative Transport

So far in this paper, the level of radiation reaching the afterbody surface has been assessed using an intensity ray normal to the surface. To obtain the actual radiative flux reaching the surface, which is the quantity required for TPS design, the intensity as function of solid angle must be integrated at each surface point. This integration is commonly approximated using the tangent slab assumption, which is known to provide a 10 - 15% over-prediction in the radiative flux on the forebody. This relatively good prediction on the

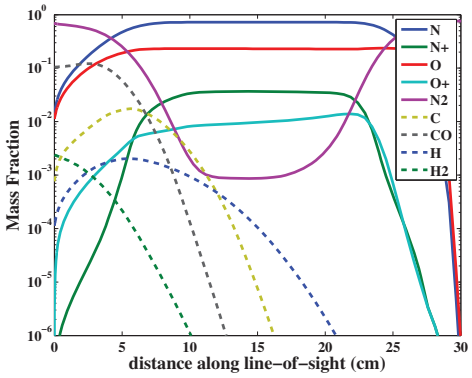


(a) Relevant Number Densities

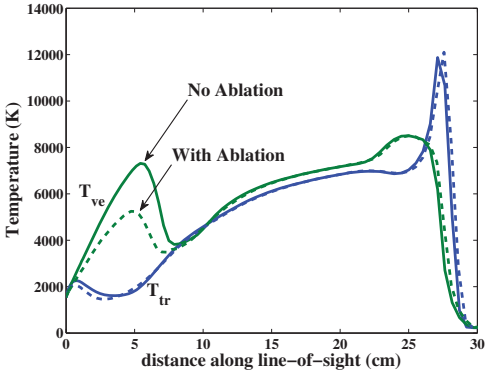


(b) Temperature Profile ($T_{ve}$ = blue, $T_{tr}$ = green)

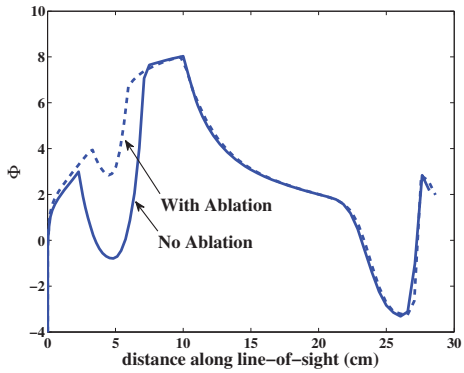


(c) $\Phi$ Profile for N

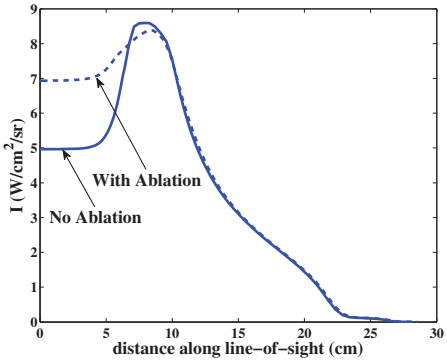


(d) Intensity Profile

**Figure 16: Radiation and flowfield properties along line-of-sight defined in Fig. 15.**

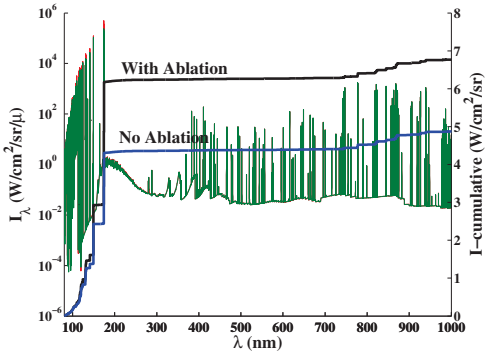


**Figure 17: Comparison of ablating and non-ablating intensity spectrum.**

forebody is expected because of the tangent-slab like flow geometry in this region (i.e. the shock layer is thin and properties vary gradually along the surface). The shoulder and afterbody regions, however, are not tangent-slab like, so the error introduced using this approximation is expected to be much larger than 10 - 15%.

To avoid the potential errors introduced by the tangent-slab approximation in the afterbody, a ray-tracing approach was developed by Mazaheri et al.,[16] which provides a rigorous integration of the intensity over the solid angle. This approach rotates axisymmetric solutions to three-dimensional solutions and interpolates numerous intensity rays through the rotated flowfield. The temperatures and number densities from these rays are input to the HARA radiation code, which solves for the radiative intensity along the given ray. This approach is used for all radiative flux values presented in this paper, unless stated otherwise.

Figure 18 presents the results of the ray-tracing and tangent-slab approaches for the Stardust 46 s case. In Fig. 18(a), the radiative flux values predicted by the two approaches are compared, while Fig. 18(b) presents the ray-tracing divided by the tangent slab value. In the forebody region, excluding the shoulder, the ray-tracing values are seen to be within the previously mentioned 15% of the tangent slab value. However, in the afterbody region near the shoulder (between 20 - 30 cm), where the afterbody radiation is largest, the ray tracing value is up to 35% less than the tangent-slab prediction. The ray-tracing prediction is lower because it accurately accounts for the weaker radiating downstream flow, whereas the tangent-slab inherently assumes the downstream flow is the same as the normal line-of-sight. Conversely, the ray-tracing approach predicts larger values above 50 cm, where the normal line-of-sight applied by the tangent-slab approach does not account for the more strongly radiating upstream flow.

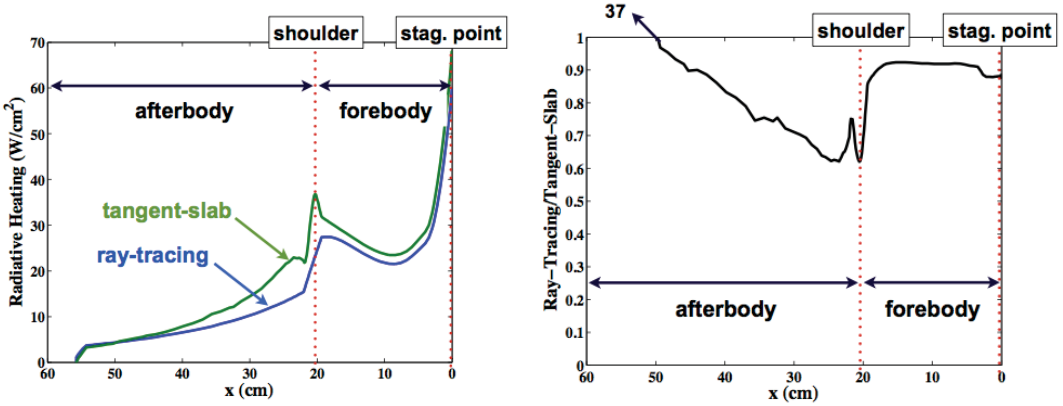


(a) Radiative Flux Comparison

(b) Ratio of Ray-Tracing and Tangent Slab Flux

**Figure 18: Comparison of ray-tracing and tangent slab radiative flux for Stardust 46 s case.**

# IV. Afterbody Radiative Heating for Stardust

To show the importance of afterbody radiative heating for a sample return capsule, this section presents the afterbody radiative and convective heating for various trajectory points of the Stardust entry. Comparisons with observed radiation measurements are also made, which provide a level of validation for the large afterbody radiative heating values presented in this work.

The trajectory points studied here are defined in Table 3. Recall that the 46 s point has been considered in examples throughout this paper. Spatial locations on the Stardust afterbody are defined in Fig. 19. Results presented here assume a fully-catalytic, radiative equilibrium wall. Although the previous section showed that forebody ablation products may increase the afterbody radiation significantly, ablation is not included in the present results. Ray-tracing is applied for all radiative flux predictions.

**Table 3: Stardust trajectory points and free-stream conditions.**

| Time (s) | Density ($kg/m^3$) | Velocity (km/s) | $T_\infty$ (K) |
|---|---|---|---|
| 38 | 2.70e-5 | 12.27 | 219 |
| 42 | 5.60e-5 | 12.06 | 221 |
| 46 | 1.00e-4 | 11.69 | 228 |
| 51 | 2.10e-4 | 10.87 | 235 |
| 53 | 2.70e-4 | 10.42 | 237 |
| 56 | 3.80e-4 | 9.62 | 243 |

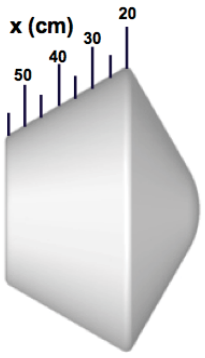


**Figure 19: Definition of afterbody locations for Stardust.**

The variation of the radiative and convective heating along the afterbody surface is presented in Fig. 20 for the 38 and 46 s trajectory points. The radiative heating is seen to be significantly larger than the convective heating over most of the afterbody surface. This significant afterbody radiation has been demonstrated in this paper to be a consequence of nonequilibrium ionization and recombination. Figure 21, which presents the time variation of the radiative and convective heating at two spatial locations, shows that radiation provides a dominant contribution to the afterbody heating over a large portion of the trajectory.

Figure 22 compares the total (radiative + convective) heating at the stagnation point and an afterbody location through the trajectory. This comparison shows that peak heating occurs earlier on the afterbody, which is dominated by radiative heating, than at the stagnation point, which is dominated by convective heating.

The Echelle radiation measurements made by Jenniskens[17] capture the radiation emitted by the shock layer towards the observing aircraft. Following the analysis presented by Liu et al,[18] comparisons with these measurements require tracing rays through the shock layer, as shown in Fig. 23, in the direction of the aircraft, followed by computing the radiative intensity along each ray and integrating over the solid angle. This approach was applied in this work for the 42 s case, resulting in the observed flux values presented in Figs. 24 and 25 (the continuum levels for the simulations were adjusted to match the measurements). The "Aft+Forebody" result represents the total prediction, while the "Forebody Only" result includes only the forebody rays defined in Fig. 23. Comparing these two values for each spectrum, it is seen that the afterbody

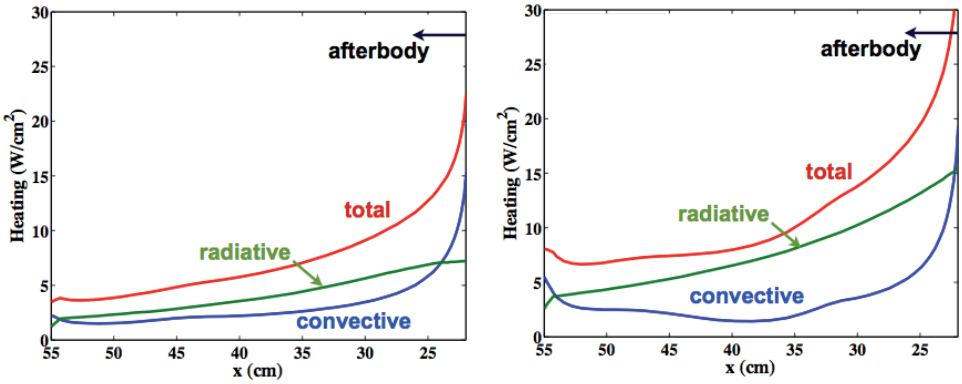


(a) t=38 s (b) t=46 s

**Figure 20: Heating components along the Stardust afterbody.**

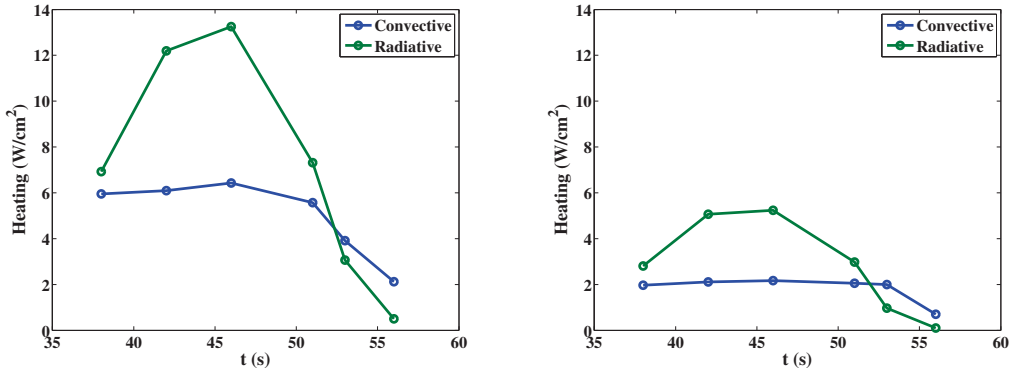


(a) x = 25 cm (b) x = 45 cm

**Figure 21: Heating throughout the Stardust trajectory.**

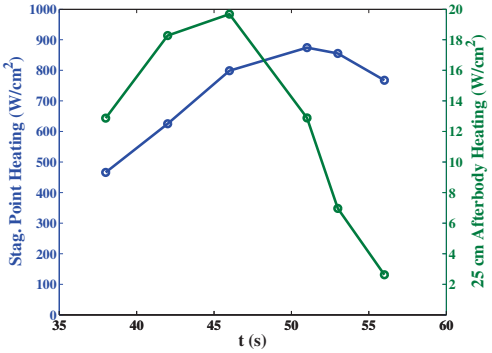


**Figure 22: Comparison of Stagnation point and afterbody ($x$=25 cm) radiative + convective heating.**

provides the dominant contribution to the observed flux. The decent agreement seen for the"Aft+Forebody" result therefore provides a level of validation for the significant afterbody radiative flux presented in this paper. The roughly 20% under-prediction seen for each spectrum is acceptable considering the uncertainties due to electron-impact ionization and escape factors discussed earlier.

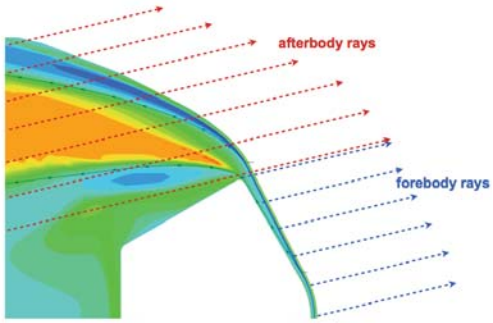


**Figure 23: Values of $\Phi$ for the 42 s case and definition of forebody and afterbody rays.**

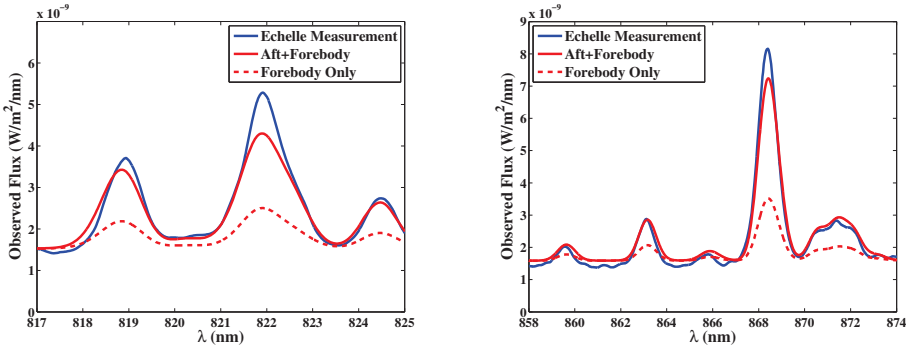


**Figure 24: Comparison between Echelle measurements and simulations for N lines.**

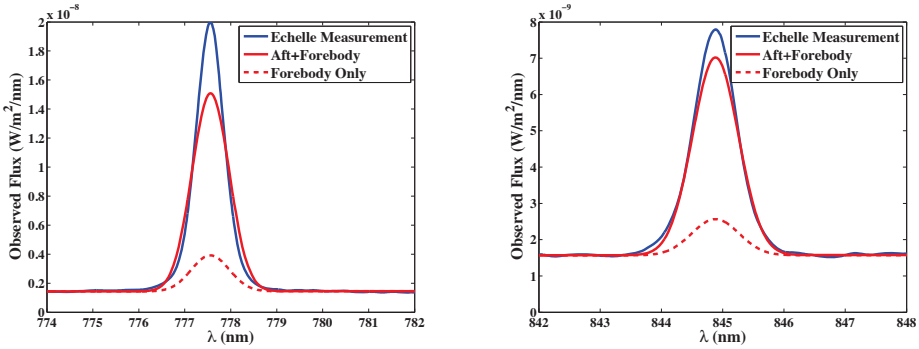


**Figure 25: Comparison between Echelle measurements and simulations for O lines.**

## V. Comparison with Fire II Afterbody Calorimeter Measurements

Because nonequilibrium radiation measurements in air are not presently available, the best experimental validation for afterbody radiative heating is provided by the Fire II calorimeter measurements. Figure 26 provides an illustration of the Fire II geometry and afterbody calorimeter locations. These calorimeters were made of gold with a 0.13 mm coating of oxidized Nichrome.[19] Unlike the Beryllium forebody calorimeters,

which have a well known wavelength-dependent absorptance that varies from roughly 0.5 in the IR to near 1.0 in the VUV, the wavelength dependent absorptance for oxidized Nichrome is unknown. Because the majority of the radiative flux in the afterbody is in the VUV, which typically has an absorptance near 1.0, a constant wavelength-independent value of 1.0 is assumed in this work.[20] This value allows the convective plus radiative heating to be compared directly to the calorimeter measurements.

Coupled flowfield-radiation solutions were obtained for each of the trajectory points listed in Table 4. While the radiative flux at the surface is computed using the ray-tracing approach, the divergence of the radiative flux is computed at each grid point in the flowfield using the tangent-slab approach. To show the impact of catalycity on the convective heating, results are presented for both a fully-catalytic and catalytic-to-ions only assumption. The wall temperature on the forebody is fixed to the measured value and radiative equilibrium is assumed on the afterbody.

**Table 4: Fire II trajectory points and free-stream conditions.**

| Time (s) | Density (kg/m$^3$) | Velocity (kms/s) | $T_\infty$ (K) | $T_w$ (K) |
|---|---|---|---|---|
| 1634 | 3.72e-5 | 11.36 | 195 | 615 |
| 1636 | 8.57e-5 | 11.31 | 210 | 810 |
| 1637.5 | 1.47e-4 | 11.25 | 228 | 1030 |
| 1639 | 2.41e-4 | 11.14 | 242 | 1325 |
| 1640.5 | 3.86e-4 | 10.97 | 254 | 1560 |

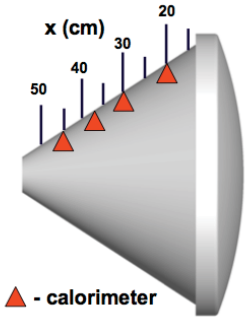


**Figure 26: Fire II geometry and calorimeter locations.**

To show the similarity between the nonequilibrium afterbody environment of the Fire II and Stardust vehicles, Fig. 27 presents the $\Phi$ values for the 1637.5 s trajectory point. These values are seen to be similar to those presented in Fig. 6 for the Stardust case, with peak values between 7 and 8. This similarity suggests that, like for Stardust, the afterbody radiative flux is significant.

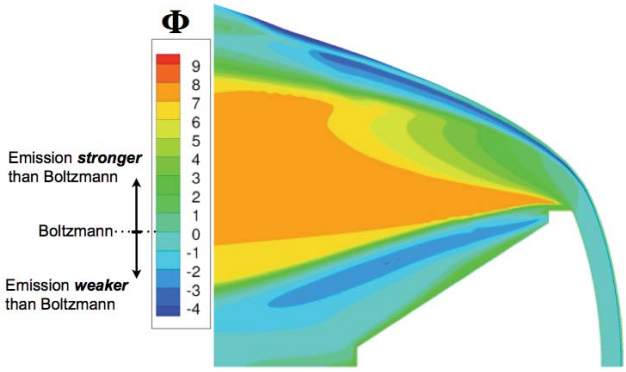


**Figure 27: Values of $\Phi$ for the Fire II case at $t$=1637.5 s**

Figures 28 and 29 compare the simulated afterbody heating with the calorimeter measurements for the 1637.5 and 1639.0 s trajectory points. The catalytic-to-ions only results are seen to under-predict the measurements, although the shape of the heating profile, which decreases slightly to a minimum and then increases, is reproduced. While the fully-catalytic predictions provide good agreement for the 20 and 30 cm calorimeters, the other two calorimeters are significantly over-predicted. Note that for even the fully catalytic result, the 20 cm calorimeter requires significant radiative heating to match the measurement. This represents a significant difference from the results of Wright et al.,[21] who show good agreement between fully-catalytic simulations without radiation and the 20 cm calorimeter measurements. Differences in two-temperature modeling, ionization rates, and the presence of radiation coupling in the present simulations are possible reasons for this discrepancy.

Because the 20 cm calorimeter is seen to encounter the lowest convective heating, this location provides the best insight into the radiative heating. To study this location further, Figure 30 compares its measured and predicted heating throughout the trajectory. Considering the fully-catalytic result, which represents the convective heating upper limit, it is seen that the convective heating alone under-predicts the calorimeter measurement for all trajectory points, therefore requiring a strong radiation contribution for agreement. When combined with the predicted radiative heating, the fully-catalytic result provides decent agreement throughout the trajectory. The heating for the catalytic-to-ions only result, which is dominated by radiation, under-predicts the measurements by as much as 50%. Regardless of the catalycity assumption, these comparisons for the 20 cm calorimeter provide evidence supporting the significant afterbody radiative heating suggested in this paper.

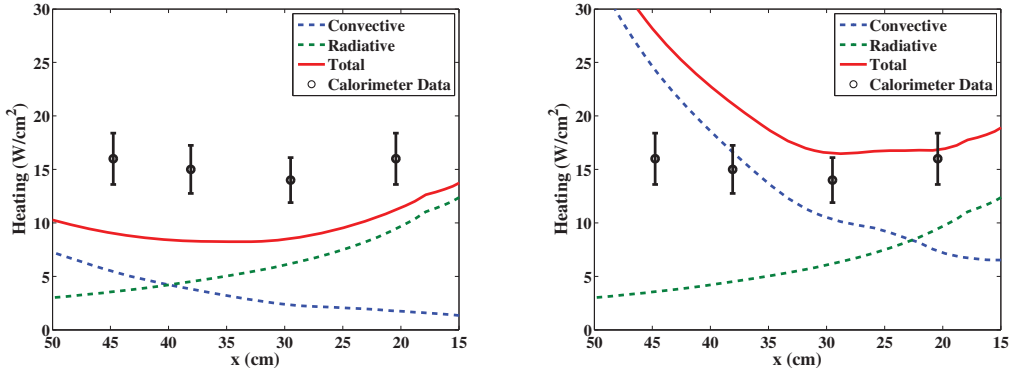


(a) catalytic-to-ions only (b) fully-catalytic

**Figure 28: Comparison of Fire II afterbody heating with calorimeter data at 1637.5 s.**

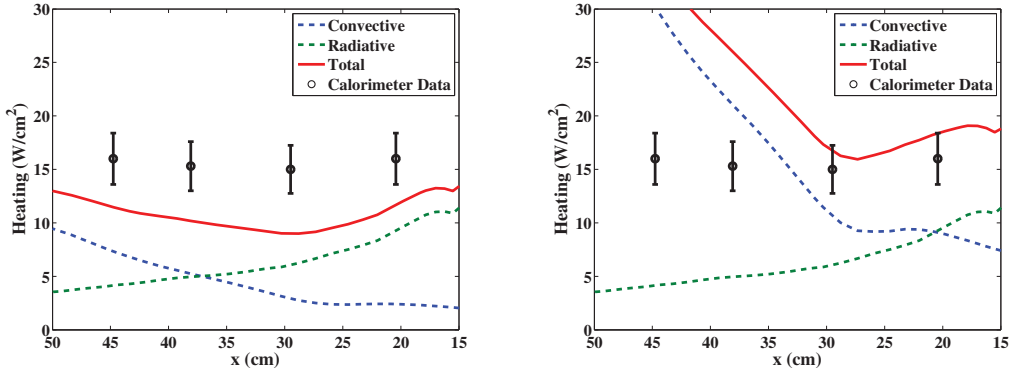


(a) catalytic-to-ions only (b) fully-catalytic

**Figure 29: Comparison of Fire II afterbody heating with calorimeter data at 1639.0 s.**

As mentioned in the Introduction, the afterbody radiometers on Fire II reported negligible values. However, because these radiometers had a lower sensitivity limit of 2 W/cm$^2$ and only measured the non-VUV

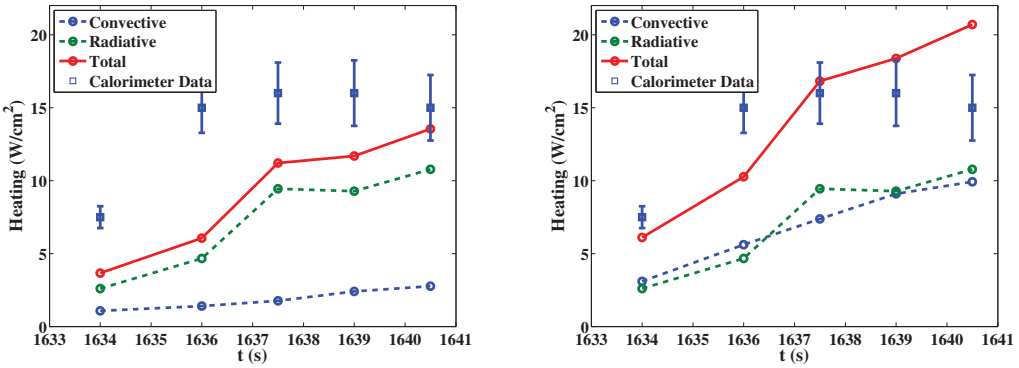


(a) catalytic-to-ions only (b) fully-catalytic

**Figure 30: Comparison of Fire II afterbody heating at the 20 cm calorimeter.**

spectrum, it was noted in the Introduction that these negligible measurements did not rule out the potential for a strong VUV-dominated radiative flux. Such a radiative flux spectrum is indeed what the present model predicts. Figure 31 presents the simulated radiative flux spectrum at the afterbody radiometer location for the 1637.5 s case, which shows a total radiative flux of 6.4 W/cm$^2$, with a non-VUV contribution of less than 2 W/cm$^2$.

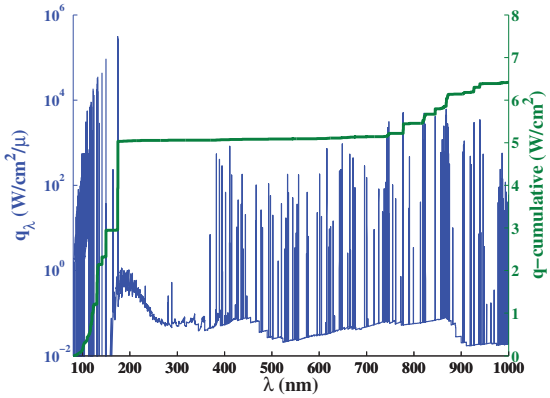


**Figure 31: Radiative flux spectrum at the Fire II afterbody radiometer location ($x$=26.6 cm).**

## VI. Conclusions

Afterbody radiative heating values are shown to be equal to, if not greater than, convective heating for Stardust-like capsules entering Earth at velocities greater than 10 km/s. A parameter $\Phi$ is defined as the logarithm of the Saha-Boltzmann population divided by the Boltzmann population. Evaluating this parameter throughout an afterbody flowfield for N allows the strongly radiating flowfield regions to be identified. Afterbody radiation predictions are shown to be sensitive to electron-impact ionization rates, escape factor modeling, and ablation products. The contribution of these modeling issues to the radiative heating uncertainty should be considered in a future study. A level of validation for these afterbody radiative heating predictions is shown to be provided by the Stardust observation measurements and Fire II calorimeters.

## VII. Acknowledgments

The present work was funded by the NASA Space Technology Mission Directorate Entry Systems and Modeling (ESM) project, with tasks leads Michael Wright and Michael Barnhardt. The authors would also

like to thank Jarvis Songer at Lockheed Martin and Todd White at ERC Corporation at NASA Ames for identifying afterbody radiation as a potential problem for Stardust-like conditions.

## References

[1]Wright, M., Milos, F., and Tran, P., "Afterbody Aeroheating Flight Data for Planetary Probe Thermal Protection System Design," *Journal of Spacecraft & Rockets*, Vol. 43, No. 5, 2006, pp. 929–943.

[2]Savajano, R., Joshi, O., and Leyland, P., "Aerothermal Analysis of the Phoebus Capsule with Radiative Heating on the Back Body," AIAA Paper 2012–1281, 2012.

[3]Shang, J. S. and Surzhikov, S. T., "Simulating Stardust Earth Reentry with Radiation Heat Transfer," *Journal of Spacecraft & Rockets*, Vol. 48, No. 3, 2011, pp. 385–396.

[4]Otsu, H., Suzuki, K., Fujita, K., and Abe, T., "Assessment of Forebody and Backbody Radiative Heating Rate of Hypervelocity Reentry Capsule," ISAS Report SP 17, 2003.

[5]Liu, Y., Prabhu, D., Sounders, D., Vinokur, M., and Dateo, C., "Comparison of Tangent Slab Approximation and Full Angular Integration in Computing Radiative Heating for the CEV Heatshield," NASA TN/EG CAP-06-124, 2006.

[6]Johnston, C. O., Hollis, B. R., and Sutton, K., "Spectrum Modeling for Air Shock-Layer Radiation at Lunar-Return Conditions," *Journal of Spacecraft & Rockets*, Vol. 45, Sep.-Oct. 2008, pp. 865–878.

[7]Wiese, W. L., Fuhr, J. R., and Deters, T. M., "Atomic Transition Probabilities of Carbon, Nitrogen, and Oxygen," *Journal of Physical and Chemical Reference Data Monograph*, , No. 7, 1996.

[8]Park, C., "Comparison of Electron and Electronic Temperatures in a Recombining Nozzle Flow of Ionized Nitrogen Hydrogen Mixture. Part 1. Theory," *Journal of Plasma Physics*, Vol. 9, 1973, pp. 187–215.

[9]Munafo, A., Lani, A., Bultel, A., and Panesi, M., "Modeling of Non-Equilibrium Phenomena in Expanding Flows by means of a Collisional-Radiative Model," *Physics of Plasmas*, Vol. 20, 2013, pp. 073501.

[10]Bourdon, A. and Vervisch, P., "Three-Body Recombination Rate of Atomic Nitrogen in Low Pressure Plasma Flows," *Physical Review E*, Vol. 54, No. 2, 1996, pp. 1888–1898.

[11]Park, C., "Effect of Lyman Radiation on Nonequilibrium Ionization of Atomic Hydrogen," AIAA Paper 2004–2277, 2004.

[12]Park, C., *Nonequilibrium Hypersonic Aerothermodynamics*, Wiley, 1st ed., 1990.

[13]Gupta, R. N., Yos, J. M., Thompson, R. A., and Lee, K.-P., "A Review of Reaction Rates and Thermodynamic and Transport Properties for an 11-Species Air Model for Chemical and Thermal Nonequilibrium," NASA RP 1232, 1990.

[14]Mcbride, B. J., Zehe, M. J., and Gordon, S., "NASA Glenn Coefficients for Calculating Coefficients for Calculating Thermodynamic Properties of Individual Species," NASA TP 2002–211556, 2002.

[15]Johnston, C. O., Brandis, A. M., and Sutton, K., "Shock Layer Radiation Modeling and Uncertainty for Mars Entry," AIAA Paper 2012–2866, 2012.

[16]Mazaheri, A., Johnston, C., and Sefidbakht, S., "Three-Dimensional Radiation Ray-Tracing for Shock Layer Radiative Heating Simulations," *Journal of Spacecraft & Rockets*, Vol. 50, No. 3, 2013, pp. 485–493.

[17]Jenniskens, P., "Observations of the Stardust Sample Return Capsule Entry with a Slitless Echelle Spectrograph," *Journal of Spacecraft & Rockets*, Vol. 47, No. 5, 2010, pp. 718–735.

[18]Liu, Y., Prabhu, D., Trumble, K. A., Saunders, D., and Jenniskens, P., "Radiation Modeling for the Reentry of the Stardust Sample Return Capsule," *Journal of Spacecraft & Rockets*, Vol. 47, No. 5, 2010, pp. 741–752.

[19]Slocumb, T. H., "Project Fire II Afterbody Temperature and Pressures at 11.35 Kilometers Per Second," NASA TM X 1319, Dec. 1966.

[20]Lueckel, W. J. and Huttinger, R. C., "The Determination of the Emissivity of Materials," Pratt and Whitney Report 2206, Dec. 1962.

[21]Wright, M., Loomis, M., and Papadopoulos, P., "Aerothermal Analysis of the Project Fire II Afterbody Flow," *Journal of Thermophysics and Heat Transfer*, Vol. 17, No. 2, 2003, pp. 240–249.